China Ocean Eng., 2022, Vol. 36, No. 5, P. 667–681
DOI: https://doi.org/10.1007/s13344-022-0060-5, ISSN 0890-5487
http://www.chinaoceanengin.cn/ E-mail: coe@nhri.cn

Hydroelastic Investigation on A Pile Breakwater Integrated with A Flexible Tail for Long-Wave Attenuation

ZHANG Chong-wei[a], ZHUANG Qian-ze[a], LI Jin-xuan[a], HUANG Luo-feng[b], NING De-zhi[a, *]

[a] State Key Laboratory of Coastal and Offshore Engineering, Dalian University of Technology, Dalian 116024, China

[b] School of Water, Energy and Environment, Cranfield University, Cranfield MK43 0AL, United Kingdom

Received March 7, 2022; revised May 29, 2022; accepted June 30, 2022

Abstract

A novel concept of wave attenuator is proposed for the defense of long waves, through integrating a flexible tail to the lee-side surface of a pile breakwater. The flexible tail works as a floating blanket made up of hinged blocks, whose scale and stiffness can be easily adjusted. A two-phase-flow numerical model is established based on the open-source computational fluid dynamics (CFD) code OpenFOAM to investigate its wave attenuation performance. Incompressible Navier−Stokes equations are solved in the fluid domain, where an additional computational solid mechanics (CSM) solver is embedded to describe the elastic deformation of the floating tail. The coupling of fluid dynamics and structural mechanics is solved in a full manner to allow assess of wave variation along the deforming body. The accuracy of the numerical model is validated through comparison with experimental data. Effects of the flexible tail on performance of the pile breakwater are investigated systematically. Dynamic behaviours of the tail are examined, and characteristics of its natural frequency are identified. For safety reasons, the wave loads impacting on the main body of the pile breakwater and the stress distribution over the tail are specially examined. It is found that both the length and stiffness of the tail can affect the wave-attenuation performance of the breakwater. A proper choice of the length and stiffness of the tail can greatly improve the long-wave defending capability of the pile breakwater. The maximum stress over the flexible tail can be restrained through optimising the deformation and stiffness of the tail.

Key words: wave attenuator, pile breakwater, OpenFOAM, fluid-structure interaction, wave transmission, coastal protection

Citation: Zhang, C. W., Zhuang, Q. Z. Li, J. X., Huang L.F., Ning, D. Z., 2022. Hydroelastic investigation on a pile breakwater integrated with a flexible tail for long-wave attenuation. China Ocean Eng., 36(5): 667–681, doi: https://doi.org/10.1007/s13344-022-0060-5

1 Introduction

With the dramatic increase in the maritime traffic and vessel size, offshore berthing is becoming increasingly important for more ports in recent decades. Breakwaters that can protect the anchorage from the action of powerful waves are within the key fundamental infrastructures of coastal engineering. In offshore deep-water locations with poor soil conditions (e.g. with a lack of a rocky bottom), the construction of conventional rubble mound breakwater is neither economical nor environment-friendly (Vijay et al., 2020; Huang and Chen, 2020). Alternatively, the pile breakwater is often considered as a competitive solution (He and Huang, 2014). A pile breakwater usually consists of an impermeable wave blocker near the free surface supported on steel or concrete piles, which is designed based on the physical fact that the wave energy decreases exponentially from the free surface downward (Brossard et al., 2003). Unlike various gravity breakwaters that can completely prevent the lower water flow, the pile breakwater allows free exchange of bottom water and sediments, which brings much less negative impact on the environment. Beyond that, the pile breakwater, as a combination of modular substructures, is easy to be prefabricated, transported and installed in engineering practice, hence reducing its construction cost to a great extent. However, these advantages of the pile breakwater are essentially established at the expense of its wave defense capability.

In recent decades, a number of studies have put great

Foundation item: This work is financially supported by the National Natural Science Foundation of China (Grant No. 51739010), the Natural Science Foundation of Liaoning Province (Grant No. 2021-MS-122), the Special Project of Guangdong Science and Technology Department (Grant No. 2021A05227), the Dalian Science and Technology Project (Grant No. 2020RQ004), and the Fundamental Research Funds for the Central Universities (Grant No. DUT22LAB128).

*Corresponding author. E-mail: dzning@dlut.edu.cn

efforts to further improve the hydrodynamic performance of classical pile breakwaters. Sundar and Subba rao (2002) proposed a pile breakwater with a quadrant solid front face on the seaside, and experimentally studied its wave transmission/reflection properties and the force experienced in regular waves. Ramnarayan et al. (2020) compared the hydrodynamic performance of curved and vertical front face pile-supported breakwaters in regular waves. Neelamani and Rajendran (2002) studied the wave transmission, reflection and energy dissipation characteristics of partially submerged T-type breakwaters using physical models, and found the transmission coefficient generally decreasing with increased wave steepness. The T-shaped floating breakwater was later investigated by Deng et al. (2019) using the matched eigen-function expansion method. The presence of the baffle was found to decrease the resonance frequency of both surge and pitch motions of the breakwater. Koutandos and Prinos (2011) numerically and experimentally studied the wave interaction with a partially immersed box-type breakwater with a plate attached at the front part of the structure. Effects of the plate on attenuation of the incident waves were discussed. Christensen et al. (2018) studied the effect of different damping mechanisms of a box-type floating breakwater. The cross section of the breakwater with wing plates can reduce the motions of the breakwater to the largest extend, while the cross section with wing plates and porous media attached to the sides can reduce the reflection and transmission most effectively. Brossard et al. (2003), in experiments, found that the wave reflection capacity of a fixed semi-submerged caisson breakwater can be effectively improved through installing an absorbing caisson at the seaside of the structure. Rageh and Koraim (2010) considered a vertical wall with permeable lower part used as a breakwater, where a theoretical model based on the eigen-function expansion method was used to study its hydrodynamic performance in regular waves. Li et al. (2020) examined the hydro-elastic interaction between water waves and a flexible submerged perforated semi-circular breakwater based on linear potential theory. Liu and Wang (2020) studied the wave-attenuation performances and hydrodynamics of moored box-type floating breakwaters with different cross-sections, using the smoothed particle hydrodynamics (SPH) method. A strong relationship was identified between the motions, mooring tensions, and wave attenuation performances of the breakwater. Wang et al. (2005) considered a semi-submerged box breakwater with internal air chambers, where the opening of the chamber was set seaward below the surface. The attack of incident waves can be buffered through the air cushion effect in the chamber.

Some other studies turn to improving the deployment strategy of multiple breakwater modules in the ocean space. For example, Ji and Suh (2010) considered a multiple-row curtainwall-pile breakwater, and found the wave transmission significantly reduced by the multiple-row deployment of breakwaters, although the difference between double-row and triple-row breakwaters was marginal. Chang et al. (2012) investigated the wave diffraction of the breakwater in a V-shaped deployment using an analytical solution. Sharifahmadian and Simons (2014) modelled the nearshore wave field behind submerged breakwaters, where the spatial transmission coefficient for regular waves in the shadow region of the breakwater was predicted using artificial neural networks. Ji et al. (2017) introduced multiple rows of plane nets between double pontoons of the floating breakwater, through which the wave dissipation performance of the breakwater was observed to be improved. Cui et al. (2021) developed a coupled SPH method to simulate the wave interaction with a multi-module floating breakwater, and the results showed that this multi-module design was more effective against short waves.

Many of the aforementioned pile breakwater designs have shown to be effective in reducing the transmission strength of short waves and even in suppressing violent wave impacts through energy dissipation. However, the essential limitation of a conventional pile breakwater in defending long waves (whose wavelength can often exceed several times the maximum breadth and draught of the breakwater in deep-water regions) has not been fully solved yet. It has been well understood that the breadth of a pile breakwater is one of the key factors that can restrain the free transmission of long waves through the structure. For example, the breakwater breadth should at least be 35% of the wave length so as to ensure the wave transmission coefficient smaller than 0.5, otherwise an even narrower breakwater can be almost transparent to long waves (Dai et al., 2018). Thus, the previous modifications on localised geometry of the pile breakwater cannot help in resisting the transmission of long waves. On the other hand, significantly increasing the breadth of the pile breakwater can effectively improve its ability on resisting long waves, but, at the same time, would greatly raise up the overall engineering costs. To be specific, enlarging the breadth of a conventional pile breakwater by several times can dramatically increase the material quantity, construction difficulty, and safety requirement for such a large floating structure. How to improve the capability of pile breakwaters to resist long waves without largely increasing the scale and modifying the geometry of structure is a significant problem to solve.

This study proposes a new strategy on further improving the wave defense capability of a conventional pile-breakwater in the long-wave environment. The key idea is to integrate an extra flexible tail to the lee side of the pile breakwater, as shown in Figs. 1a and 1b. Fig. 1c is an example of how a flexible tail may look like in engineering practice (Beytlik, 2021). The flexible tail works as a floating blanket made up of hinged blocks, whose scale and stiffness can be easily adjusted. For convenience of expression, the integrated system that contains the original pile breakwater and the flexible

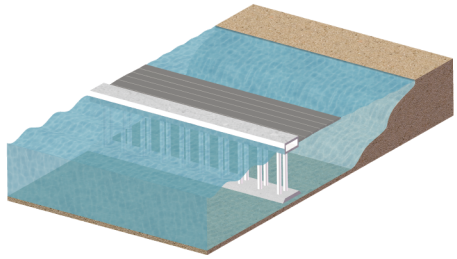

(a) Application scenario

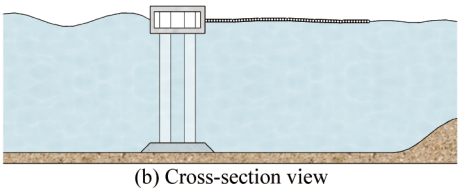

(b) Cross-section view

(c) An example of how a flexible tail looking like in practice

Fig. 1. Concept of the novel wave attenuator through integration of a flexible tail with the pile breakwater.

tail, as a whole, is referred to as the 'wave attenuator' hereafter. Accordingly, the term 'pile breakwater' specifically refers to the main breakwater structure excluding the flexible tail.

This novel design has obvious advantages. Theoretically, inevitable transmitted waves behind the pile breakwater can be further attenuated and suppressed by this long tail. Introducing such a tail essentially functions like covering a large free-surface area with a floating blanket or plate. According to theoretical analyses in Shugan et al. (2012), an optimally designed horizontal flexible plate can be an effective wave barrier, especially for cases with wave lengths smaller than the plate length. The stiffness of the tail can be easily controlled by adjusting the tightness of the hinges. Meanwhile, introducing such a floating tail does not change the original design of the pile breakwater, which is especially applicable to existing pile breakwaters. The tail can be fixed on the leeside of the pile breakwater, so that no additional mooring system is required to restrain the drift motion. The scale and coverage of the tail can be adjusted easily, depending on the wave conditions to be considered. Thus, the additional increase in cost to the pile breakwater can be greatly squeezed. Like some cases of flexible breakwaters (Wu et al., 2002; Dai et al., 2018), the tail can even be made up of recycled materials such as waste tires.

In this study, a numerical model based on the open-source CFD code OpenFOAM is established to investigate the hydrodynamic performance of this novel design in long-wave environment. Details of the methodology are introduced in Section 2. In Section 3, the benchmark model in Brossard et al. (2003) is referred to for parameter settings of the numerical simulation. The accuracy of the numerical model is validated through comparison with experimental data. Effects of the flexible tail on hydrodynamic performance of the pile breakwater are investigated. Dynamic behaviours of the tail are examined, and characteristics of its natural frequency are identified. For safety reasons, the wave loads impacting on the main body of the pile breakwater and the stress distribution over flexible tail are specially examined. Conclusions are drawn in Section 4.

2 Methodology description

This study considers a sufficiently long breakwater deployed perpendicular to the wave direction, so that hydrodynamic analyses can be simplified by focusing on the two-dimensional (2D) cross-section model. A two-phase-flow numerical wave flume is established in OpenFOAM, as shown in Fig. 2. The wave flume has dimension of the length L, the height H, and the water depth h. A wave generation zone and a wave damping zone, both with the length of L_d, are set at two ends of the wave flume, respectively. A simplified model of the wave attenuator is placed in the middle of the tank. The main body of the pile breakwater near the free surface is box-shaped, with the breadth L_b, the draught D, and the total height H_b. The model of the flexible tail is simplified as an elastic plate model fixed on the lee side of the pile breakwater and floating on the free surface, and the length and thickness of which are L_a and d, respectively. The flow-blocking effects of underwater piles are out of consideration, which suggests that conclusions drawn from the present numerical study are more conservative for practical designs. A Cartesian coordinate system O-xy is established with O at the lower-left corner of the flume, O-x axis pointing horizontally to the right, and O-y axis upwards.

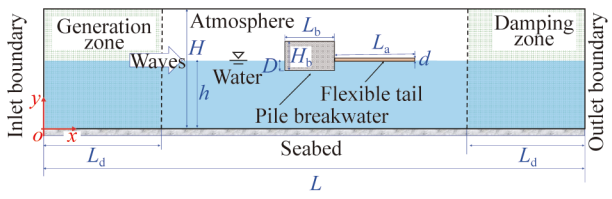

Fig. 2. Sketch and parameters of the numerical wave flume.

For numerical simulations, the left boundary of the wave flume is set as the velocity inlet. The top is the atmospheric boundary. Both the flume bottom and surfaces of the pile breakwater are fixed walls. Surfaces of the tail are free deformation boundaries. The computational domain is divided into the fluid and solid sub-domains. In the fluid sub-domain, the following incompressible Navier−Stokes equations are solved

$$\nabla \cdot \boldsymbol{v} = 0; \tag{1}$$

$$\rho\left(\frac{\partial \boldsymbol{v}}{\partial t} + \boldsymbol{v}\cdot\nabla\boldsymbol{v}\right) = -\nabla P + \rho g + \nu\rho\nabla^2\boldsymbol{v}, \tag{2}$$

where $\boldsymbol{v}$ is the fluid velocity, P the fluid pressure, ρ the fluid density, ν the coefficient of the fluid kinematic viscosity, and t the time. The coupling of fluid's pressure and velocity is solved by the PISO (Pressure-Implicit with Splitting of Operators) algorithm (Issa, 1986). In the solid sub-domain, the deformation of the elastic plate is determined by the nonlinear Saint-Venant-Krichhoff hypder-elasticity law as:

$$\rho_{\mathrm{s}}\int_{V_0}\frac{\partial}{\partial t}\left(\frac{\partial \boldsymbol{u}}{\partial t}\right)\mathrm{d}V-\oint_{S_0}\boldsymbol{n}\cdot(2\mu+\lambda)\nabla\boldsymbol{u}\mathrm{d}S=\oint_{S_0}\boldsymbol{n}\cdot\boldsymbol{q}\mathrm{d}S+\rho_{\mathrm{s}}\int_{V_0}\boldsymbol{g}\mathrm{d}V \tag{3}$$

with

$$\boldsymbol{q}=\mu(\nabla\boldsymbol{u})^{\mathrm{T}}+\lambda\mathrm{tr}(\nabla\boldsymbol{u})\boldsymbol{I}-(\mu+\lambda)\nabla\boldsymbol{u}+\mu\nabla\boldsymbol{u}\cdot(\nabla\boldsymbol{u})^{\mathrm{T}}+\frac{1}{2}\lambda\mathrm{tr}\left[\nabla\boldsymbol{u}\cdot(\nabla\boldsymbol{u})^{\mathrm{T}}\right]\boldsymbol{I}+\boldsymbol{W}\cdot\nabla\boldsymbol{u}; \tag{4}$$

$$\boldsymbol{W}=2\mu\boldsymbol{K}+\lambda\mathrm{tr}(\boldsymbol{K})\boldsymbol{I}; \tag{5}$$

$$\boldsymbol{K}=\frac{1}{2}\left[\nabla\boldsymbol{u}+(\nabla\boldsymbol{u})^{\mathrm{T}}+\nabla\boldsymbol{u}\cdot(\nabla\boldsymbol{u})^{\mathrm{T}}\right]; \tag{6}$$

$$\mu=\frac{E}{2(1+\vartheta)}; \tag{7}$$

$$\lambda=\frac{\vartheta E}{(1+\vartheta)(1-2\vartheta)}, \tag{8}$$

where ρ_{s} is the density of the solid, $\boldsymbol{u}$ the displacement vector, $\boldsymbol{I}$ the second-order unit tensor, $\boldsymbol{n}$ the unit normal vector on the surface pointing outward, $\boldsymbol{W}$ the second-order Piola−Kirchhoff stress tensor according to the nonlinear Saint−Venant−Kirchhoff hyper-elasticity law (Tuković et al., 2018; Cardiff et al., 2018), μ and λ the Lame constants related to the Young's modulus E and the Poisson's ratio ϑ, and $\boldsymbol{K}$ the Green-Lagrange strain tensor. Variables with the subscript 0 refer to those at the mean location.

The finite volume method (FVM) is used to solve these governing equations. Both the fluid and solid sub-domains are discretized into unstructured quadrilateral grids, where the fluid dynamic quantities are centered on the centroid of each grid cell. The gradient, convection, and Laplacian terms in the governing equations are discretized into arithmetic expressions using the Gaussian linear scheme, the Gauss upwind scheme, and the Gaussian linear correction scheme, respectively. The solver has second-order accuracy in both space and time.

The free surface in the flume is traced by the volume of fluid (VOF) method (Hirt and Nichols, 1981). To be specific, a scalar field α is defined in the computational domain. In each grid cell, the value of α represents the volume fraction of the liquid phase (with $\alpha=0$ and $\alpha=1$ for the gas and liquid phases, respectively). The free surface can be found in a cell with $0<\alpha<1$. The velocity, density, and dynamic viscosity coefficient in each free-surface cell can be obtained through the following linear approximation

$$\boldsymbol{v}=\alpha\boldsymbol{v}_{\mathrm{a}}+(1-\alpha)\boldsymbol{v}_{\mathrm{b}}; \tag{9}$$

$$\rho=\alpha\rho_{\mathrm{a}}+(1-\alpha)\rho_{\mathrm{b}}; \tag{10}$$

$$\mu=\alpha\mu_{\mathrm{a}}+(1-\alpha)\mu_{\mathrm{b}}, \tag{11}$$

where the subscripts a and b refer to the phases of liquid and gas, respectively. Water waves in the flume are then generated and absorbed using the opensource toolbox 'waves2Foam' (Jacobsen et al., 2012). To be specific, waves are generated by setting the velocity inlet boundary condition. By referring to Larsen et al. (2019), the time derivative term is calculated by Crank-Nicolson (CN) scheme, with the mixing factor $\psi=0.3$. The relaxation technique is used at the wave generation and damping zones, in order to avoid the secondary wave reflection from the inlet and outlet boundary of the flume. With the relaxation technique, the velocity field $\boldsymbol{v}$ at every time step is adjusted as follows:

$$\boldsymbol{v}=(1-\omega_{\mathrm{R}})\boldsymbol{v}_{\mathrm{ref}}+\omega_{\mathrm{R}}\boldsymbol{v}_{\mathrm{sol}}, \tag{12}$$

where ω_{R} is the weighting factor, $\boldsymbol{v}_{\mathrm{ref}}$ is the target fluid velocity, and $\boldsymbol{v}_{\mathrm{sol}}$ is the computed fluid velocity. The value of ω_{R} ranges from 0 to 1 in the wave generation zone and from 1 to 0 in the damping zone, and is set constant 1 in the rest of the wave flume.

At any instant, the instantaneous deformation of the elastic plate and fluid flows determine each other. A fully two-way coupling fluid−solid interaction (FSI) algorithm is applied. As shown in Fig. 3, at each time step, a predicted deformation of the elastic plate is first given based on solutions at the previous time step, and grids of both the solid and fluid sub-domains are updated accordingly. Then, Navier−Stokes equations are solved, and fields of the pressure and velocity in the fluid can be obtained. After that, hydrodynamic loads over surfaces of the plate model are calculated, and the governing equation of the solid sub-domain is solved. The accuracy of the newly obtained deformation of the plate is evaluated through comparison with the predicted one. If satisfied accuracy is reached, the simulation moves forward to the next time step. Otherwise, the procedure is iterated by replacing the predicted deformation with the newly obtained one until convergence. In this way, physical

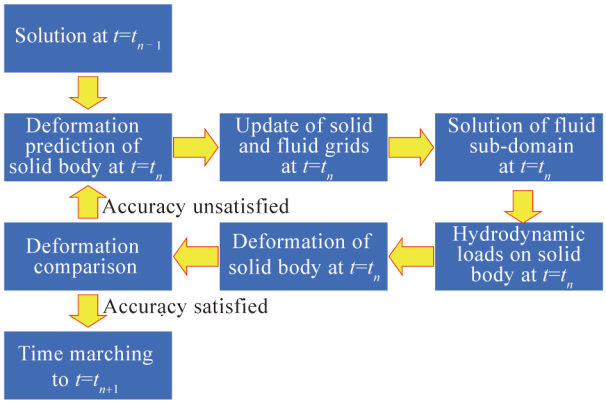

Fig. 3. Procedure of the fully two-way coupling fluid−solid interaction (FSI) algorithm at each time step.

quantities of the solid and fluid sub-domains are synchronised.

Variable time steps are used for time marching with the maximum Courant number C_{max} set as 0.1. The Courant number is defined as (Li and Zhang, 2019):

$$C = \frac{|\boldsymbol{U}|\Delta t}{\Delta l}, \tag{13}$$

where $|\boldsymbol{U}|$ is the maximum velocity field in the fluid field, Δt is the time step, and Δl is the size of the grid cell along the direction of the maximum fluid velocity. With the principle, the time step can be small enough to prevent numerical divergences.

The original OpenFOAM solver was proposed by Tuković et al. (2018) , although it was only applicable to single-phase-flow problems. Huang (2017) developed the present two-way coupling fluid−solid interaction algorithm in two-phase-flow numerical wave flumes. The solver was subsequently used to investigate hydroelasticity problems of ice floes (Huang et al., 2019) and submerged breakwaters (Huang and Li, 2022). In this study, the two-way coupling algorithm is further extended to cases with both rigid and elastic structures in water waves.

3 Results and discussions

The benchmark model in Brossard et al. (2003) is referred to for parameter settings of the numerical simulation, with L = 9.45 m, H = 0.5 m, h = 0.25 m, L_d = 1.8 m, L_b = 0.45 m, H_b = 0.2 m, and D = 0.08 m. The flexible tail has the thickness d = 0.03 m, the density 500 kg/m^3, and the Poisson's ratio 0.3. The wave height is fixed to be H_w = 0.03 m for all cases.

3.1 Convergence test and validation of numerical model

Convergence tests on the grid discretization of the numerical model are first conducted in this subsection. As an example of illustration, a flexible tail with the length L_a = L_b and the Young's modulus E = 50 MPa is considered. For water wave simulations, sufficiently fine grids must be deployed over the free surface space. Hereafter, this study takes the shortest wavelength λ_{min} and wave height H_w for reference to set the grid size of the fluid sub-domain, and L_a and d for the grid size of the solid sub-domain. As described in Table 1, three sets of grids are established for comparison, where Δx and Δy denote the horizontal and vertical grid sizes, respectively. Local grid refinements are further carried out in the computational domain around the structure. From Grid-1 to Grid-3, the grid fineness is improved and the number of cells increases from 25552 to 149852. Detailed arrangement of grids in both the fluid and solid sub-domains around the wave attenuator can be found in Fig. 4.

Table 1 Sizes of three sets of grids for convergence study

Grid-index	Grid size in fluid sub-domain	Grid size for solid sub-domain
1	$\Delta x = \lambda_{min}/50$, $\Delta y = H_w/6$	$\Delta x = L_a/23$, $\Delta y = d/3$
2	$\Delta x = \lambda_{min}/100$, $\Delta y = H_w/10$	$\Delta x = L_a/45$, $\Delta y = d/5$
3	$\Delta x = \lambda_{min}/150$, $\Delta y = H_w/14$	$\Delta x = L_a/68$, $\Delta y = d/8$

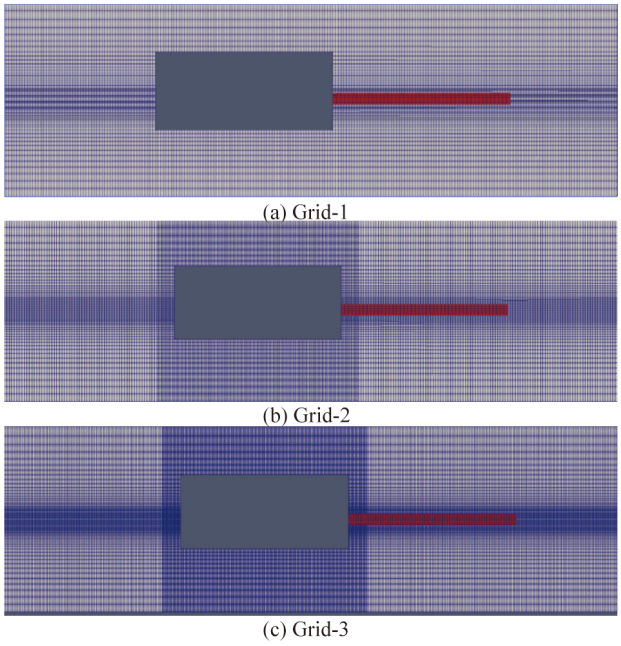

Fig. 4. Local grid refinement of (a) Grid-1, (b) Grid-2 and (c) Grid-3, in which computational solid mechanics (CSM) grids are in red.

Incident waves with the minimum wavelength λ_{min}= $1.5L_b$ are taken for example. Based on grids of different finenesses, the calculated histories of wave force acting on the front wall of the pile breakwater are compared in Fig. 5a, and the free-surface profiles at $t = 30T$ between x = $(3.5-6.5)\lambda_{min}$ of the numerical wave flume are shown in Fig. 5b. Hereafter, T is used to denote the period of incident waves. In both figures, as the number of grid cells increases, the wave forces and free-surface profiles both converge quickly. The difference between results of Grid-2 and Grid-3 is too small to affect the conclusions drawn from the numerical simulations. Therefore, to accelerate the simulations, Grid-2 is used for subsequent numerical simulations. With Grid-2, 100 cells are deployed in the range of each wave length. For even longer waves, such grid size can also guarantee the numerical accuracy without difficulty.

A reference time step is set for each case of simulation. At each time step, the Courant number C is checked. If C exceeds a critical value (e.g. C_{max} = 0.1 here), the time step is adjusted to guarantee the condition of $C < C_{max}$. Otherwise, Δt is assigned with the reference time step. Fig. 6a compares histories of the wave force acting on the front wall of the pile breakwater by setting the reference time step as Δt = 0.0005 s, 0.001 s, and 0.002 s, respectively. Fig. 6b gives the comparison of corresponding wave profiles at t/T = 30. It shows that, as the reference time step is refined from Δt = 0.002 to 0.0005 s, the results converge efficiently. With considerations on both numerical accuracy and time consumption, Δt = 0.001 s can be used as the reference time

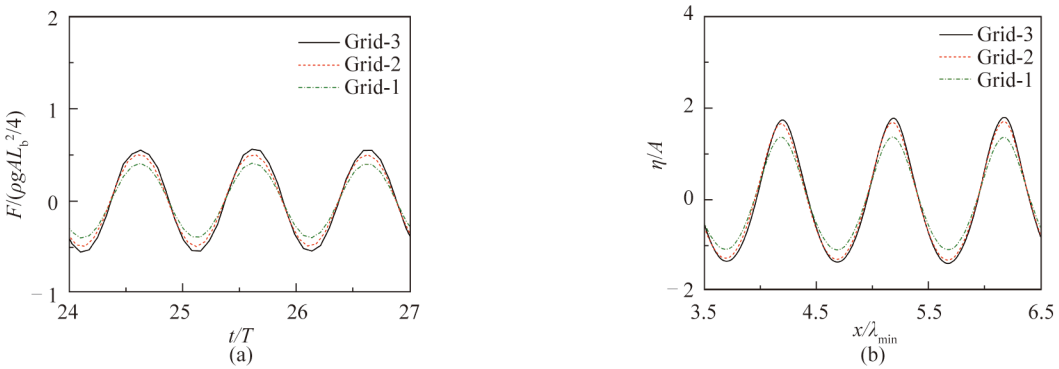

Fig. 5. Comparison of (a) histories of wave forces acting on the front wall of the pile breakwater and (b) wave profiles at $t/T = 30$, based on grids of different fineness.

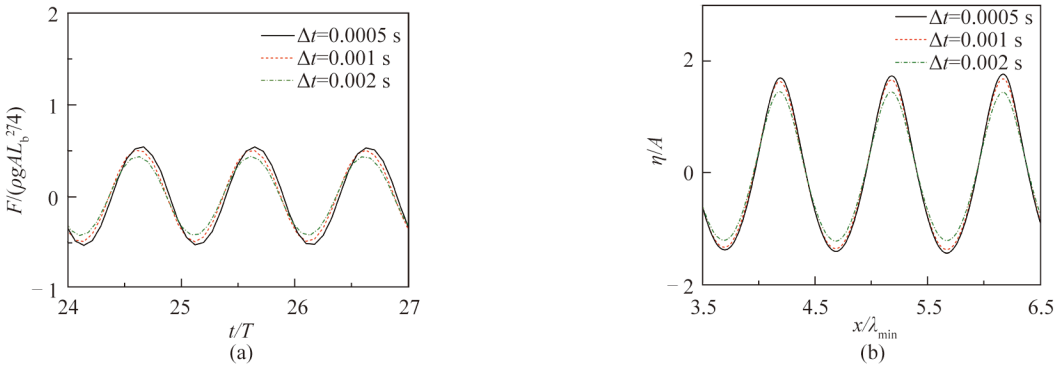

Fig. 6. Comparison of (a) histories of wave forces acting on the front wall of the pile breakwater and (b) wave profiles at $t/T = 30$, with different reference time steps.

step for cases in this study.

To validate the accuracy of the present numerical model, the physical experiments carried out in Brossard et al. (2003) are reproduced. According to the reference (Brossard et al., 2003), a barge-type pile breakwater is fixed in the wave flume, and transmitted and reflected waves through the structure are measured. Compared with the physical model in experiments, the present breakwater has a very short tail at the lee-side of the breakwater, in order to examine solvers of the same numerical wave flume developed for the wave attenuator. To approximate the experimental model to the largest extent, the present numerical model reduces the length of the wave attenuator down to $L_a = 0.02$ m and the thickness d to 0.0152 m. The flexible tail has the cross-sectional area of 0.3% that of the pile breakwater, which is not expected to affect the hydrodynamic performance of the pile breakwater. Fig. 7 compares the calculated hydrodynamic coefficients (i.e the wave transmission coefficient $K_t = H_t/H_w$ and the wave reflection coefficient $K_r = H_r/H_w$) of the pile breakwater with those measured in experiments. Here, the reflected wave height H_r is obtained using the two-point method (Goda and Suzuki, 1976), where two wave gauges are deployed at 1.0 and 1.1 times the wavelength away from the weather side of the breakwater. The transmitted wave height H_t is identified through fast Fourier Transform

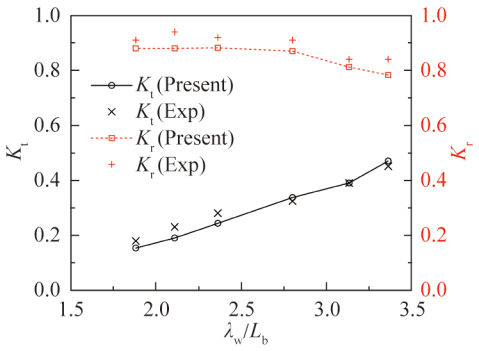

Fig. 7. Comparison of the calculated transmission and reflection coefficients of the pile breakwater with those measured in experiments.

(FFT) analyses, where the height of the dominant wave component corresponding to the incident wave frequency is taken as H_t. It shows that, under all wave conditions into consideration, the calculated hydrodynamic coefficients generally agree well with the corresponding experimental data, which has confirmed the reliability of the present numerical model. Meanwhile, this figure also shows that as the wavelength of incident waves increase up to over three times the breadth of the breakwater, the wave transmission coefficient increases rapidly towards 0.5. This is an evidence that, the pile breakwater has limitations on defending long

waves.

To further examine wave loads on the pile breakwater, experimental cases in Rodríguez and Spinneken (2016) are also reproduced by the present solver. The numerical wave flume is similar to that built for Brossard et al. (2003), in which parameters are set as L = 11 m, h = 1.25 m, L_d = 3 m, H_w = 0.05 m and k = 4. In Fig. 8, the obtained dimensionless vertical wave loads on the pile breakwater are compared with the experiment data, where the transversal width of the pile breakwater is W = 2.76 m. The overall trends and amplitudes of the numerical and experimental results have a good agreement. Therefore, the present model of numerical wave flume can be reliable for the calculation of wave loads.

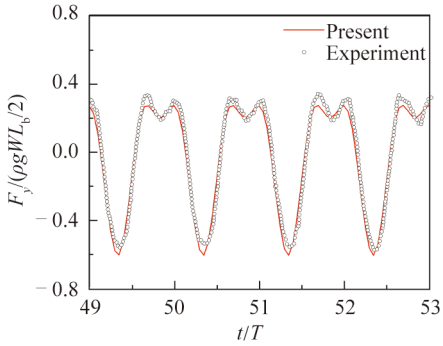

Fig. 8. Comparison of the calculated vertical wave loads of the pile breakwater with those measured in experiments.

3.2 Hydrodynamic performance of wave attenuator

From this subsection on, effects of the flexible tail on hydrodynamic performance of the pile breakwater are investigated. The length and stiffness of the flexible tail are the main focus of this study. Long waves with L_w/L_b ranging from 1.5 to 3.5 are considered. Two groups of case set-ups are established, with parameters shown in Table 2. Group I includes Cases 2-1, 2-2 and 2-3, where the length of the tail is fixed, but the Young's modulus varies from E = 50, 500 to 5000 MPa. For the flexible tail in practice, the Young's modulus can be adjusted based on the hinge stiffness of adjacent floating units. In Group II, the length of the tail varies from 5% to 2.0 times the breadth of the pile breakwater (corresponding to Case 0-2 to Case 4-2, respectively), while the Young's modulus is kept constant as E = 500 MPa. It should be noted that Case 0-2 can be considered as a traditional pile breakwater without the flexible tail, since the value of L_a is sufficiently small compared with the size of the breakwater.

Table 2 Parameters for the case study

Group	Case	L_a/L_b	E (MPa)
I	2-0	1.0	0
	2-1	1.0	50
	2-2	1.0	500
	2-3	1.0	5000
II	0-2	0.05	500
	1-2	0.5	500
	2-2	1.0	500
	3-2	1.5	500
	4-2	2.0	500

The cases in Group I are first considered. Fig. 9 shows effects of the tail with different stiffness values on the transmission coefficient of the pile breakwater. It shows that the wave transmission through the pile breakwater is severer in longer waves, which is true no matter the flexible tail exists or not. Under the shortest incident wave condition with λ/L_b = 1.5, the stiffness or even the existence of the tail has little effect on the transmission coefficient of the breakwater. In even longer waves, the flexible tail can obviously reduce the transmission coefficient of the breakwater. Increasing the stiffness of the tail can further reduce the wave transmission under these long-wave conditions into consideration. Meanwhile, when a stiffer tail is adopted, the increasing ratio of the transmission coefficient with the wave length is smaller. It is also noticed that the transmission coefficients with E = 500 and 5000 MPa are almost identical. As Young's modulus of the tail increases up to 500 MPa, any further increase of the tail stiffness cannot further reduce the wave transmission. Under each long-wave condition, as the stiffness of the tail increases, the wave transmission coefficient decreases quickly. The decrease ratio of K_t against Young's modulus is larger in longer waves. Under the worst condition with λ_w/L_b= 3.5, the wave transmission coefficient can reduce by about 0.2. Thus, under long-wave conditions, an ideally rigid tail can have better performances in resisting long waves, compared with traditional pile breakwater without the flexible tail. By using a sufficiently long and fully-rigid plate, the free surface oscillation is suppressed to be still. In practice, for a large floating plate, the stiffness of the tail should not be too large, in order to avoid large stresses that can cause structural failures. Therefore, it is acceptable to select the flexible tail with Young's modulus of 500 MPa, with respect to the present pile breakwater model.

Fig. 10 shows effects of the flexible tail with different

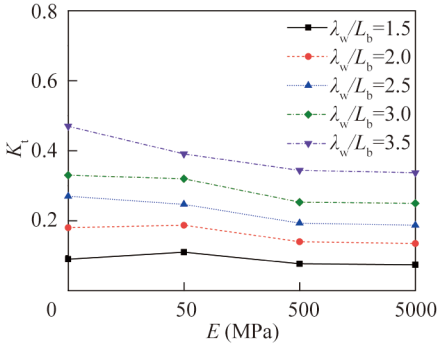

Fig. 9. Effect of flexible tail with different Young's modulus values on transmission coefficients of the pile breakwater.

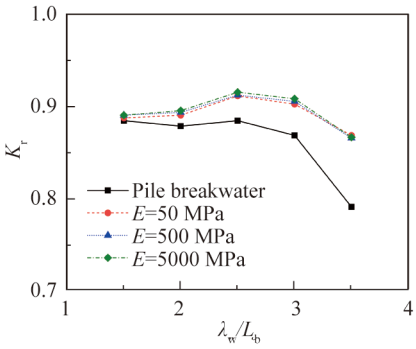

Fig. 10. Effect of flexible tail with different Young's modulus values on reflection coefficients of the pile breakwater.

Young's modulus values (E = 50 MPa, 500 MPa or 5000 MPa) on reflection coefficients of the pile breakwater. Without flexible tails, the reflection coefficient does not change much for waves with $1.5L_b \leqslant \lambda_w \leqslant 2.5L_b$, but reduces rapidly with a further increase of the incident wavelength. Under the wave condition of $\lambda_w = 3.5L_b$, the reflection coefficient becomes smaller than 0.8. With a flexible tail, the reflection coefficient of the breakwater generally increases under wave conditions with $\lambda_w \geqslant 2.0L_b$. The reflection coefficient reaches the maximum in waves with $\lambda_w = 2.5L_b$. Compared with the case of the pile breakwater, the wave reflection effect is greatly strengthened by equipping with a flexible tail, particularly in long waves. The flexible tail serves as a breadth extension of the breakwater. However, among cases of E = 50 MPa, 500 MPa or 5000 MPa, the stiffness of the flexible tail does not show evident effects on the reflection coefficient.

Fig. 11 shows the corresponding dissipation coefficients (i.e. $K_d = 1-K_r^2-K_t^2$) of the pile breakwater when the flexible tail is assigned with different Young's modulus values. It shows that, even for the pile breakwater, the dissipation coefficient is not constantly zero. An important source of the energy dissipation is likely to be the vortex shedding at the leeward corner of the breakwater. With the flexible tail being installed, violent vortices can be suppressed, leading to a reduced dissipation coefficient. For all cases either with or without flexible tails, the dissipation coefficient of the breakwater is smaller in longer waves. This is because a larger proportion of longer waves is likely to be transmitted to the far end of flexible tail, rather than locally constrained and dissipated near the breakwater. Comparing the results with E = 50 MPa, 500 MPa and 5000 MPa suggests that the structural damping may also contribute to the energy dissipation. With E = 500 MPa and 5000 MPa, the flexible tail has little difference on the dissipation coefficient.

Then, we fix the stiffness of the flexible tail with E = 500 MPa, and investigate effects of its length on transmission coefficients of the pile breakwater. Results obtained from Case 0-2 to Case 4-2 are compared in Fig. 12. The transmission coefficient of the breakwater increases with the incident wavelength increase as expected, regardless of the length of the tail. With L_a/L_b = 0.5, 1.0 and 1.5, the tail generally has similar wave dissipation performance. In the longest wave (with λ_w/L_b = 3.5), the flexible tail with L_a/L_b = 1.0 can effectively reduce the transmission coefficient of the pile breakwater from over 0.5 down to about 0.3. This confirms the effectiveness of the flexible tail in resisting long waves. Meanwhile, it is interesting to find that, as the length of the tail increases from 0 to $2L_b$, the wave transmission first decreases and then increases. This applies to all wave conditions into consideration. The best wave defending effect is achieved when the length of the tail equals to that of the pile breakwater. In other words, the choice of the tail's length is not the longer the better. There exists some complex interaction between the flexible tail and water waves, which would be further discussed in subsequent subsections. Even so, the wave dissipation effect in cases with the longest tail is still better than that without installing the tail. Based on these facts, to achieve the best wave defending effect in long waves, the lengths of the flexible tail and the main body of the pile breakwater can be set to be the same, for the model into consideration.

Fig. 13 shows effects of the flexible tail with different lengths on the reflection coefficient of the breakwater. As the length of the flexible tail increases from zero to $2L_b$, the reflection coefficient first increases and then decreases with

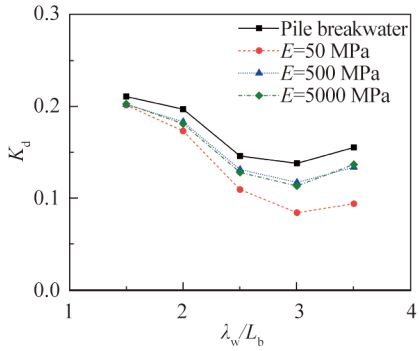

Fig. 11. Effect of flexible tail with different Young's modulus values on dissipation coefficients of the pile breakwater.

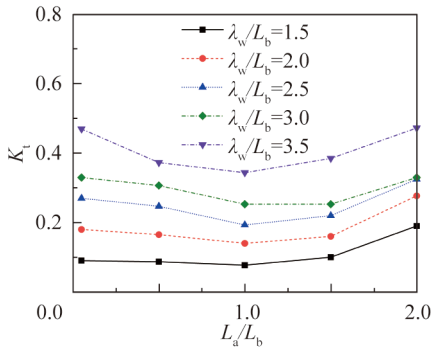

Fig. 12. Effect of flexible tail with different lengths on transmission coefficients of the pile breakwater.

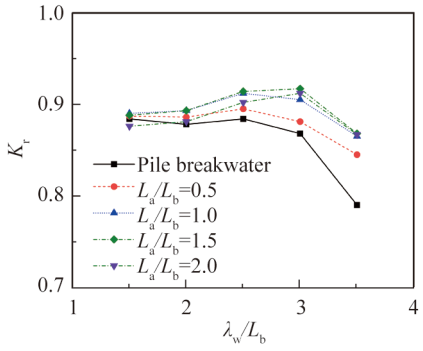

Fig. 13. Effect of flexible tail with different lengths on reflection coefficients of the pile breakwater.

the wavelength. A longer flexible tail tends to cause a larger reflection coefficient. Fig. 14 depicts the dissipation coefficients of the breakwater, corresponding to different lengths of flexible tails. The energy dissipation in the flow field is evidently reduced when a longer tail is used.

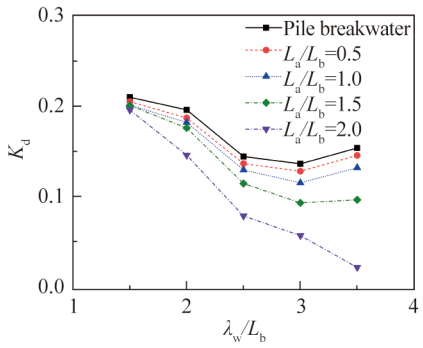

Fig. 14. Effect of flexible tail with different lengths on dissipation coefficients of the pile breakwater.

3.3 Hydroelastic behaviour of flexible tail

An interesting observation in Subsection 3.2 is that a longer flexible tail does not necessarily guarantee a better wave dissipation performance. To figure out what happens in the longer tail, dynamic behaviours of the tail are examined in this subsection. The flexible tail with $L_a/L_b = 2.0$ and E = 500 MPa in incident waves with $\lambda_w/L_b = 3.5$ is first taken for example.

Fig. 15 shows the deformation of the tail at eight instants in one period from $t = 15T$ to $15T+7T/8$. For illustration purpose, the deformation of the tail is amplified by ten times in the vertical direction in the figure. The tail oscillates in the form of the cantilever plate around the equilibrium position, mainly in the fundamental oscillation mode. Correspondingly, the largest displacement can be found at the free edge of the tail, i.e. the position marked by 'A'. The instantaneous distribution of the stress over the tail is also shown in colour, which will be further discussed in subsequent subsections. Fig. 16 gives an example of the displacement history measured at the free edge of the tail.

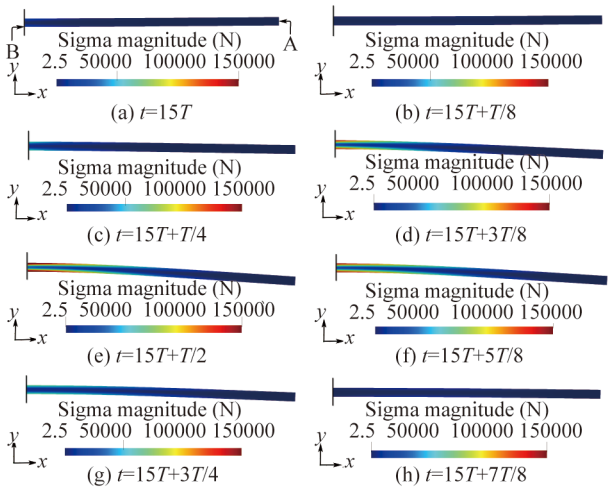

Fig. 15. Deformation and stress distribution of the wave attenuator, with $L_a/L_b = 2$, E = 500 MPa, and $\lambda_w/L_b = 3.5$.

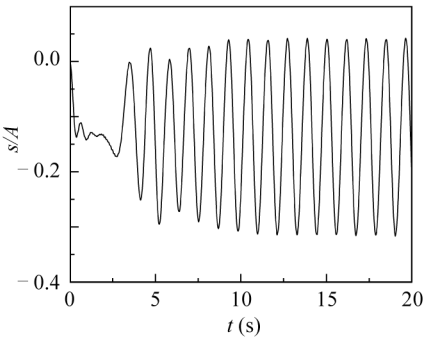

Fig. 16. Displacement history measured at the free edge of the flexible tail for Case 4-2 in waves with $\lambda_w = 3.5L_b$.

Hereafter, $s(t)$ is used to denote the instantaneous vertical displacement. It shows that, as the incident waves arrive, the flexible tail first oscillates irregularly and then falls in to the steady stage. The difference between the upper and lower envelopes of the displacement history in the steady stage is referred to as the displacement amplitude. The steady oscillations of the floating tail are associated with free surface disturbances behind the tail.

This subsection further compares the displacement amplitudes measured at the free edge of the tail in the steady stage for cases with different tail lengths, as shown in Fig. 17a. For all cases into consideration, the maximum displacement amplitude of the flexible tail is always smaller than 20% of the incident wave amplitude. Under each wave condition, the oscillation amplitude at the free edge of the tail increases sharply with the increase of the tail length. For the tail with $L_a/L_b \leqslant 1.0$, the displacement amplitude at Point A does not increase evidently in even longer waves. Correspondingly, a less evident oscillation of the tail can lead to a smaller wave disturbance behind the breakwater. In Fig. 17b, we further vary the Young's modulus of the flexible tail and investigate the displacement amplitude measured at

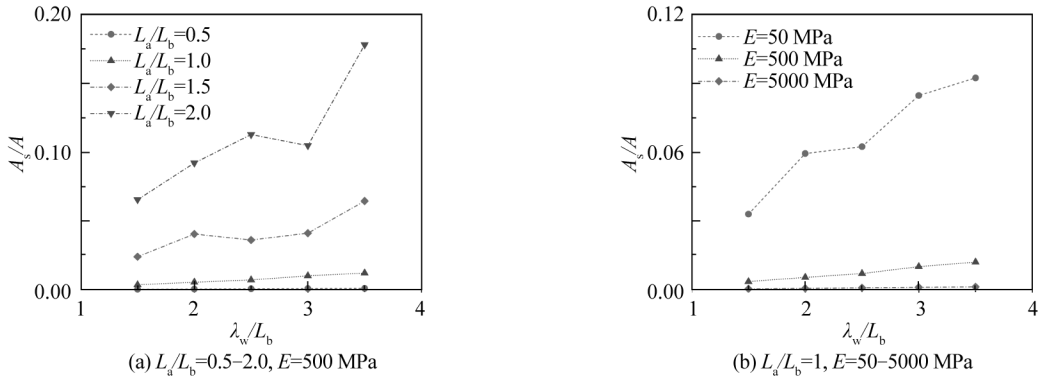

Fig. 17. Displacement amplitude measured at the free edge of the flexible tail in the steady stage with: (a) L_a/L_b = 0.5−2.0 and E = 500 MPa; (b) L_a/L_b = 1 and E = 50−5000 MPa.

the free edge of the tail in the steady stage, corresponding to cases in Group I. It is evident that a stiffer tail corresponds to a smaller oscillation amplitude of the tail, which can be expected.

Therefore, the flexible tail does not always enhance the wave defence capability of the pile breakwater. A proper length and stiffness of the tail must be selected to avoid large amplitude oscillations of the tail and subsequently free surface disturbances.

3.4 Natural frequency identification of flexible tail

From the above analyses, it is observed that, as incident waves pass through the breakwater, the flexible tail may first undergo a transient stage of oscillations for several periods, before it reaches the stage with steady oscillations at the wave frequency. Fig. 18 is an example that depicts displacement histories of the free edge of the tail under the action of different incident waves, for Case 2-2 with E = 500 MPa and $L_a = L_b$. The tail first oscillates at a relatively high frequency, with the oscillation amplitude decreasing with time. Then, a lower-frequency oscillation component of the tail rises and reaches the steady stage after a sufficiently long time.

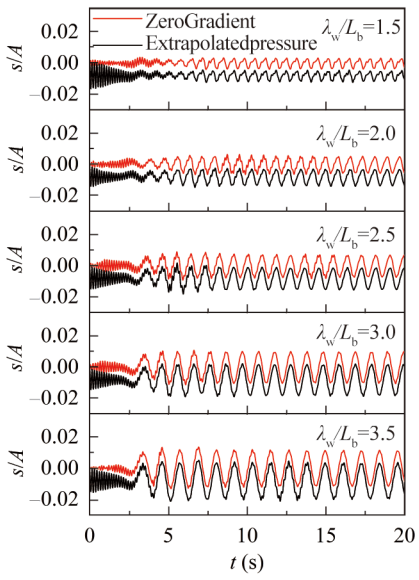

Fig. 18. Comparison of displacement history measured at the free edge of the flexible tail for Case 2-2 in different incident waves under two boundary conditions.

Through an in-depth investigation, the transient oscillation is found to be first induced by an initial imbalance between the gravity and buoyancy forces. With the VOF method, the free surface cannot be recognized as a sharp interface but is treated as a transition layer. For a thin flexible tail, the buoyancy is sensitive to the resolution of the free surface layer. When one end of the flexible tail is firmly fixed on the stationary breakwater, a net force between the gravity and buoyancy can drive an initial vibration of the flexible tail. However, due to the damping of the fluid-structure system, the initial vibration disappears quickly, so that the flexible tail can finally reach an equilibrium position.

Through a series of numerical trials, it is found that the initial imbalance is sensitive to settings of the boundary condition on the flexible tail. Fig. 18 compares displacement histories at the free edge of the flexible tail for Case 2-2 in different incident waves, where two different boundary conditions are applied on the flexible tail. The “zeroGradient”, referring to a zero-gradient pressure condition from the fluid field onto the tail surface, corresponds to an inner extrapolation of the fluid field. The “extrapolatedPressure” corresponds to a boundary condition that performs both an inner extrapolation of the flow field and an outer calculation depending on the values of the solid field calculation. With these two boundary conditions, the obtained oscillation amplitude of the flexible tail is not affected evidently, but its position of equilibrium alters. Compared with the “extrapolatedPressure” condition, the “zeroGradient” condition provides a better calculation of the initial buoyance, and the equilibrium position is on the still free surface. Even so, the “zeroGradient” condition does not erase initial vibrations completely, and the gravity and buoyancy forces cannot be perfectly identical based on the numerical resolution.

The transient oscillations at the initial stage are associated

with the physical properties of the flexible tail itself, particularly with the natural oscillation period. The fast Fourier transform (FFT) operation is conducted in the initial stage of these displacement histories in Fig. 19. The initial spectra of the tail in different waves are given in Fig. 20a. It shows that under the action of different incident wave, the dominant vibration frequency of tail is invariable (i.e. f_a = 6.6 Hz). Thus, the natural frequency of the flexible tail is recognised as f_a. The natural oscillation frequency of tail is much higher than the wave frequencies. Fig. 20b further gives the frequency spectra of the displacement histories in the steady stage. At this time, the tail mainly oscillates at the dominant frequency of the incident wave. The double-frequency component $2f_w$ can also be observed, although with a much smaller value compared with that of the f_w component. The contribution of the natural frequency component f_a can be omitted, which means that the flexible tail has reached a 'forced oscillation' state in the steady stage.

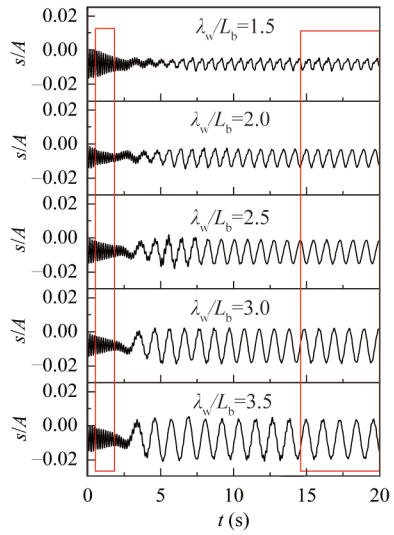

Fig. 19. Displacement history measured at the free edge of the flexible tail for Case 2-2 in different incident waves.

Figs. 21a and 21b further take cases in Groups I and II, respectively, to show effects of the structural stiffness on oscillation behaviours of the flexible tail in long waves of $\lambda_w = 3.5L_b$. With the increase of the Young's modulus or the decrease of the tail length, the oscillation frequency of the tail in the initial stage is found to increase evidently, which indicates the increase of the natural oscillation frequency f_a. In the steady stage, the oscillation frequency is observed to be the same for all cases. The natural oscillation frequencies of the flexible tail with different parameters are summarised in Fig. 22. It shows that, as the length of the tail increases, its natural frequency has a logarithmic decrease. In contrast, with the increase of the stiffness of the tail, the natural frequency nearly increases with a logarithmic trend. In practical application, the natural oscillation frequency of the flexible tail must be adjusted away from the dominant wave frequency by changing the Young's modulus and the length of the tail, in order to avoid unnecessary resonances of the tail that may further disturb the water surface of the sheltering area. As to the longwave environment, it is recommended to set flexible tail with a sufficiently high natural oscillation frequency.

3.5 Wave loads on pile breakwater and stress distribution over flexible tail

In this subsection, we aim to examine the structural safety of the wave attenuator, through analyzing the wave loads on the pile breakwater and the stress distribution over

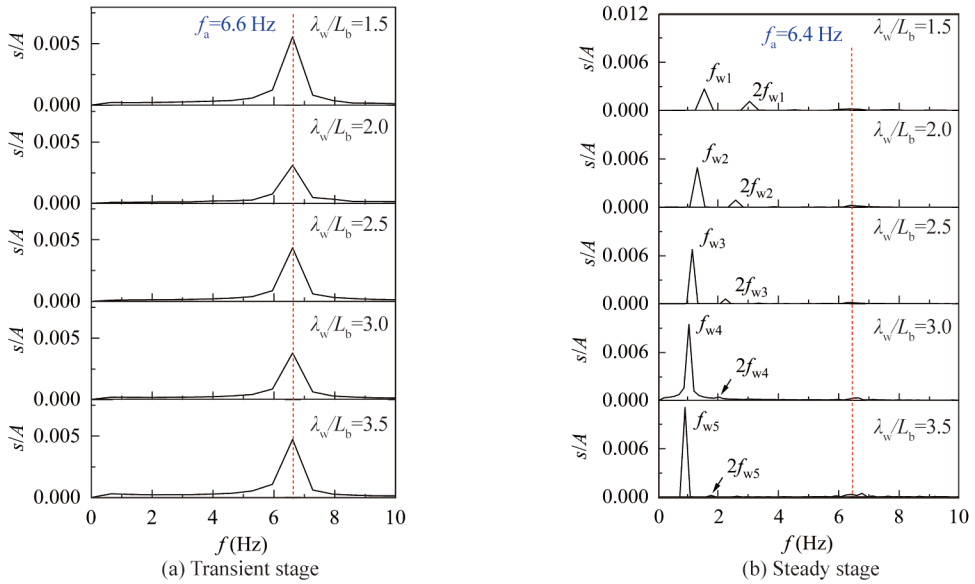

Fig. 20. Spectra of vertical displacement histories at the free edge of the flexible tail for Case 2-2 with different incident waves in the (a) transient stage, and (b) steady stage.

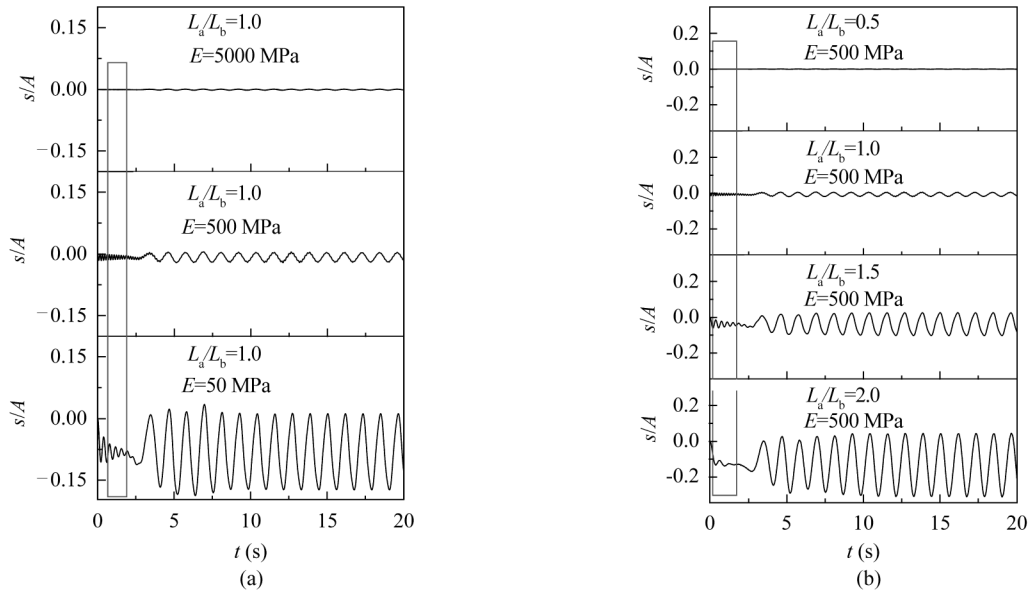

Fig. 21. Displacement history measured at the free edge of the flexible tail (a) with different values of Young's modulus and (b) different lengths in waves of $\lambda_w = 3.5L_b$.

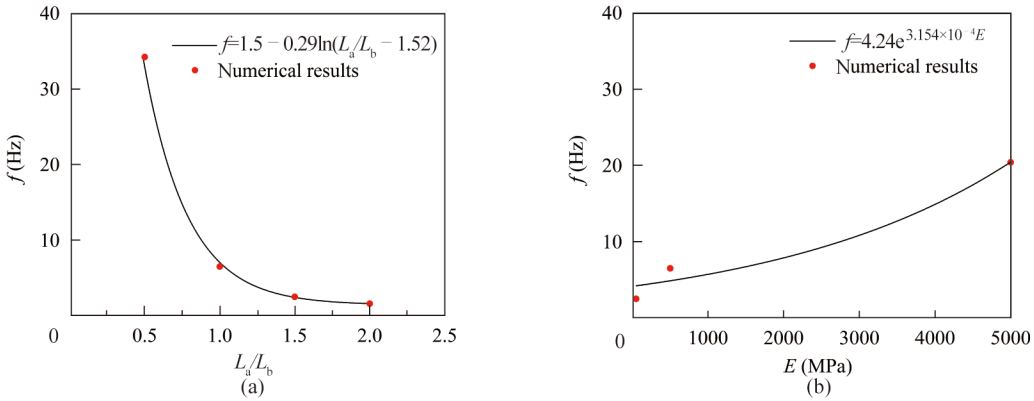

Fig. 22. Natural oscillation frequency of the flexible tail with (a) different lengths and (b) Young's modulus values.

flexible tail. Effects of the existence of the flexible tail on the total wave force F_a at the weather side of the pile breakwater are first investigated. The wave force F_b acting on the front surface of the breakwater without the tail is taken for reference. Fig. 23a gives the force ratio F_a/F_b corresponding to cases in Group I. It shows that, with the flexible tail being installed, the wave force on the weather-side surface of the pile breakwater is slightly smaller in shorter incident waves, but larger in longer waves. The ratio of F_a/F_b rises in a longer incident wave. Even so, the existence of the flexible tail brings smaller than 10% increment of the wave loads at most. Under each wave condition, the stiffness of the tail does not change the wave loads acting on the front surface of the breakwater. Fig. 23b further shows the force ratio F_a/F_b corresponding to cases in Group II when the flexible tail has different lengths. With a shorter tail, the existence of the tail has less effects on wave forces acting on the front surface of the pile breakwater. The maximum value of the force ratio is always smaller than 1.1 for cases into consideration. In general, the existence of the tail does not cause extra large wave forces on the pile breakwater. In other words, the flexible tail has limited effects of wave loads acting on the front surface of the breakwater.

The stress distribution along the flexible tail in each case is further considered. The tail is rigidly fixed at lee side of the breakwater in the form of cantilevers. Thus, as the tail oscillates in the steady state, the maximum stress always appears at the lower-left corner of the tail when its free edge reaches the largest displacement. Fig. 24a is an example of the stress history measured at the lower-left corner of the tail for Case 4-2 in waves with $\lambda_w = 3.5L_b$. It shows that the lower-left corner is always experiencing a suppression stress. The maximum stress tends to be constant in the steady stage, which is obtained for further analyses. In Fig. 24a, strong

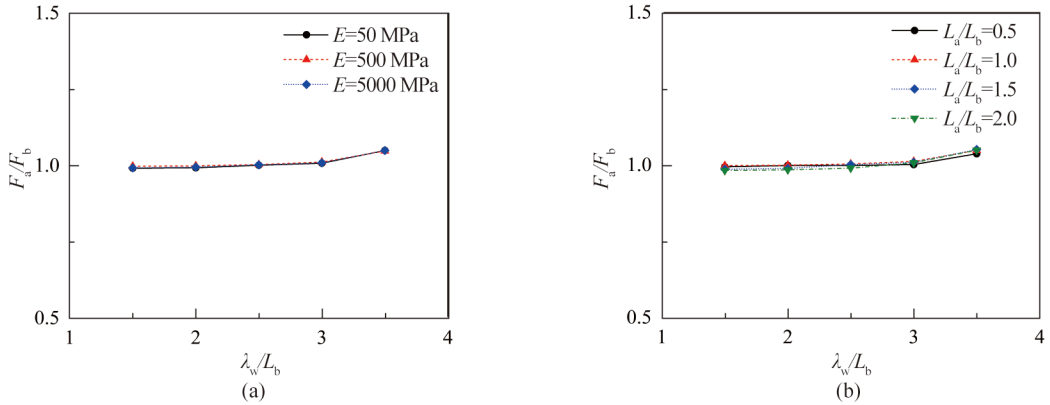

Fig. 23. Wave loads on the main body of the pile breakwater with (a) different values of Young's modulus of the flexible tail and (b) different lengths.

nonlinear components featured with higher-frequency oscillations can be noticed in the history of stress. Through a fast-Fourier analysis, the spectrum of the history can be obtained, as given in Fig. 24b. Non-negligible high-order components at two, three, four, and even five times the wave frequency (i.e. $2f_w$, $3f_w$, $4f_w$, and $5f_w$) can be recognized. By referring to the natural oscillation frequency (i.e. f_a) of the flexible tail, it can be told that f_a is very close to two times the wave frequency. According to the second-order Stokes wave theory, water waves in the present nonlinear wave flume contain both f_w and $2f_w$ components. In other words, the condition of $f_a = 2f_w$ is reached for the present case. It is believed that the $2f_w$ wave component must have triggered the nonlinear vibration resonance of the flexible tail here. Systematic tests are also carried out for waves with $1.5L_b \leqslant f_w < 3.5L_b$, but similar higher-order frequency components are not observed.

In Fig. 25, the maximum stress on the flexible tail in the steady stage is given for cases in Groups I and II. By referring back to Fig. 17, it can be found that the maximum stress here is correlated to the displacement and Young's modulus of the tail. Fig. 25a shows that, for a stiffer tail with E over 500 MPa, the maximum stress increases with the wavelength increase almost linearly. With a smaller stiffness (e.g. E = 50 MPa), the maximum stiffness of the tail does not vary largely for long waves with $\lambda > 2L_b$. Fig. 25b shows that, with E = 500 MPa, the maximum stress increases with the length of the tail under each wave condition, and long incident waves tend to cause larger stress on the tail.

It should be mentioned that, within the linear potential-flow theory, whether deploying the flexible tail at the seaward or leeward side of the breakwater does not change the wave attenuation effect of the present system. However, from the safety and economic points of view, it is better to deploy the flexible tail at the leeward side. Otherwise, the flexible tail has to endure large bending moments or buckling loads, and becomes easier to damage. A frequent maintenance of the damaged tail violates the original purpose of cost saving.

4 Conclusions

This study proposes a design of wave attenuator, as a new strategy for pile breakwaters to improve their hydrodynamic performance in defending long waves. A flexible tail made up of multiple floating units is integrated to the lee side of the pile breakwater. A two-phase-flow numerical model based on open-source codes is established to investigate the wave-attenuation performance of this novel design. The computational domain is divided in two sub-domains corresponding to the fluid and solid solvers, respectively. Incompressible Navier−Stokes equations are solved in the

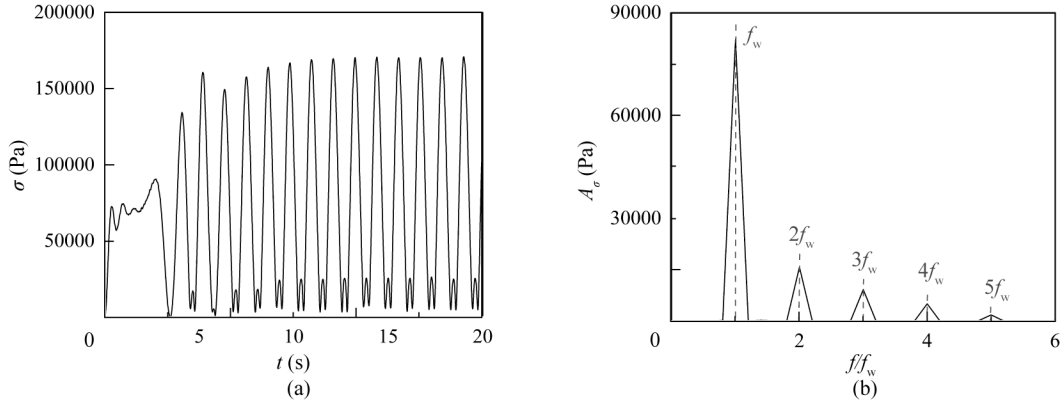

Fig. 24. (a) Histories of stress at the lower-left corner of the flexible tail for Case 4-2, and (b) corresponding spectrum.

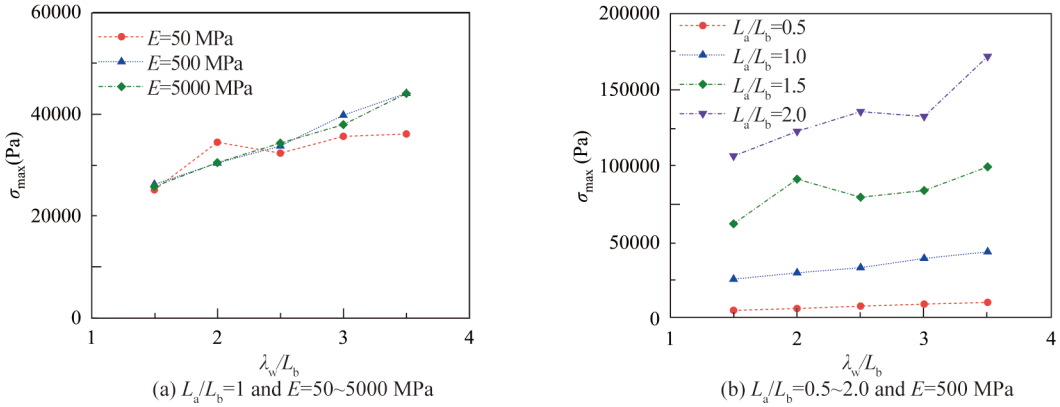

Fig. 25. Maximum stress of the flexible tail in the steady stage.

fluid domain, where the nonlinear Saint−Venant−Krichhoff hypder-elasticity law is adopted to describe the deformation of the flexible tail. The instantaneous information transfer between the fluid and solid sub-domains is solved by specially introducing a fully two-way coupling FSI algorithm. The numerical model is verified through a series of convergence tests and further validated by comparing its results with experimental data.

Effects of the flexible tail on the wave-attenuation performance of the pile breakwater are investigated. Two groups of case set-ups are established, with focus on the length and stiffness of the tail. It is confirmed that the wave transmission through the pile breakwater is severer in longer waves, no matter the flexible tail exists or not. Under the shortest incident wave conditions, the stiffness or even the existence of the flexible tail has little effect on the transmission coefficient of the breakwater. However, when the wavelength increases up to 1.5 times the breadth of the breakwater, the flexible tail can effectively reduce the transmitted waves passing through the breakwater. Besides, increasing the tail stiffness can help further reduce the wave transmission under long-wave conditions into consideration. As Young's modulus of the flexible tail increases up to 500 MPa, any further increase of the flexible tail stiffness cannot greatly help reduce the wave transmission. In practice, the stiffness of the floating tail should not be too large, to avoid potential structural failures due to large stresses.

Meanwhile, it is also interesting to find that the choice of the tail length is not that the longer the better. Through further examination, it is found that there exists some complex interactions between the flexible tail and water waves. A too long flexible tail can oscillate in the form of cantilever plate, which can further cause free surface disturbances behind the tail. Even so, the wave dissipation effect in cases with the longest flexible tail is still better than that without installing the tail. Among cases into consideration, the best wave defending effect is achieved when the length of the flexible tail is set the same as that of the pile breakwater.

Further, detailed dynamic behaviours of the flexible tail are examined. Characteristics of its natural frequency are identified through spectral analyses on the transient oscillations of the tail in the initial stage. As the length of the flexible tail increases, its natural frequency has a logarithmic decrease. With the increase of the tail stiffness, the natural frequency nearly increases with a logarithmic trend. In practical application, the natural oscillation frequency of the flexible tail must be adjusted away from the dominant wave frequency by changing the Young's modulus and the length of the tail, in order to avoid unnecessary resonances of the flexible tail that may further disturb the water surface of the sheltering area.

For safety reasons, the wave loads impacting on the pile breakwater and the stress distribution over flexible tail are specially examined. It shows that the existence of the flexible tail brings smaller than 10% increment of the wave loads at most. Under each wave condition, the tail stiffness does not change the wave loads acting on the front surface of the pile breakwater. The maximum stress over the flexible tail is correlated to the displacement and Young's modulus of the tail. For a sufficiently stiff tail, the maximum stress increases with the wavelength increase almost linearly. The maximum stress is also found to increase with the tail length increse under each wave condition, and longer incident waves tend to cause larger stress on the flexible tail.

In conclusion, the present novel design of wave attenuator by integrating a flexible tail to the pile breakwater has been verified to be effective. A proper choice of the length and stiffness of the flexible tail can greatly help improve the long-wave defending capability of the pile breakwater. In future studies, different scales and forms of the breakwater can be taken into account, and effectiveness of the flexible tail can be tested on these breakwaters.

References

Beytlik, 2021. *Group of Sportsmen in sailboats floating by coast*, Pexels, Retrieved October 30, 2022, from https://www.pexels.com/photo/group-of-sportsmen-in-sailboats-floating-by-coast-7522007/.

Brossard, J., Jarno-Druaux, A., Marin, F. and Tabet-Aoul, E.H., 2003. Fixed absorbing semi-immersed breakwater, *Coastal Engineering*, 49(1−2), 25−41.

Cardiff, P., Karač, A., De Jaeger, P., Jasak, H., Nagy, J., Ivanković, A. and Tuković, Ž., 2018. An open-source finite volume toolbox for solid mechanics and fluid-solid interaction simulations, arXiv preprint arXiv:1808.10736. (Preprint).

Chang, K.H., Tsaur, D.H. and Huang, L.H., 2012. Accurate solution to diffraction around a modified V-shaped breakwater, *Coastal Engineering*, 68, 56–66.

Christensen, E.D., Bingham, H.B., Friis, A.P.S., Larsen, A.K. and Jensen, K.L., 2018. An experimental and numerical study of floating breakwaters, *Coastal Engineering*, 137, 43–58.

Cui, J., Chen, X. and Sun, P.N., 2021. Numerical investigation on the hydrodynamic performance of a new designed breakwater using smoothed particle hydrodynamic method, *Engineering Analysis with Boundary Elements*, 130, 379–403.

Dai, J., Wang, C.M., Utsunomiya, T. and Duan, W.H., 2018. Review of recent research and developments on floating breakwaters, *Ocean Engineering*, 158, 132–151.

Deng, Z.Z., Wang, L., Zhao, X.Z. and Huang, Z.Y., 2019. Hydrodynamic performance of a T-shaped floating breakwater, *Applied Ocean Research*, 82, 325–336.

Goda, Y. and Suzuki, Y., 1976. Estimation of incident and reflected waves in random wave experiments, *Proceedings of the 15th International Conference on Coastal Engineering*, American Society of Civil Engineers, Honolulu.

He, F. and Huang, Z.H., 2014. Hydrodynamic performance of pile-supported OWC-type structures as breakwaters: An experimental study, *Ocean Engineering*, 88, 618–626.

Hirt, C.W. and Nichols, B.D., 1981. Volume of fluid (VOF) method for the dynamics of free boundaries, *Journal of Computational Physics*, 39(1), 201–225.

Huang, J.J. and Chen, G.P., 2020. Experimental modeling of wave load on a pile-supported wharf with pile breakwater, *Ocean Engineering*, 201, 107149.

Huang, L.F., 2017. *An Opensource Solver for Wave-Induced FSI Problems*, A Course at Chalmers University of Technology, Edited by Nilsson. H., http://dx.doi.org/10.17196/OS_CFD#YEAR_2017.

Huang, L.F. and Li, Y.Z., 2022. Design of the submerged horizontal plate breakwater using a fully coupled hydroelastic approach, *Computer-Aided Civil and Infrastructure Engineering*, 37(7), 915–932.

Huang, L.F., Ren, K., Li, M.H., Tuković, Ž., Cardiff, P. and Thomas, G., 2019. Fluid-structure interaction of a large ice sheet in waves, *Ocean Engineering*, 182, 102–111.

Issa, R.I., 1986. Solution of the implicitly discretised fluid flow equations by operator-splitting, *Journal of Computational Physics*, 62(1), 40–65.

Jacobsen, N.G., Fuhrman, D.R. and Fredsøe, J., 2012. A wave generation toolbox for the open-source CFD library: OpenFoam®, *International Journal for Numerical Methods in Fluids*, 70(9), 1073–1088.

Ji, C.H. and Suh, K.D., 2010. Wave interactions with multiple-row curtainwall-pile breakwaters, *Coastal Engineering*, 57(5), 500–512.

Ji, C.Y., Cheng, Y., Yang, K. and Oleg, G., 2017. Numerical and experimental investigation of hydrodynamic performance of a cylindrical dual pontoon-net floating breakwater, *Coastal Engineering*, 129, 1–16.

Koutandos, E.V. and Prinos, P.E., 2011. Hydrodynamic characteristics of semi-immersed breakwater with an attached porous plate, *Ocean Engineering*, 38(1), 34–48.

Larsen, B.E., Fuhrman, D.R. and Roenby, J., 2019. Performance of interFoam on the simulation of progressive waves, *Coastal Engineering Journal*, 61(3), 380–400.

Li, A.J., Liu, Y., Li, H.J. and Fang, H., 2020. Analysis of water wave interaction with a flexible submerged perforated semi-circular breakwater, *European Journal of Mechanics-B/Fluids*, 79, 345–356.

Li, X. and Zhang, W., 2019. 3D numerical simulation of wave transmission for low-crested and submerged breakwaters, *Coastal Engineering*, 152, 103517.

Liu, Z.Q. and Wang, Y.Z., 2020. Numerical studies of submerged moored box-type floating breakwaters with different shapes of cross-sections using SPH, *Coastal Engineering*, 158, 103687.

Neelamani, S. and Rajendran, R., 2002. Wave interaction with T-type breakwaters, *Ocean Engineering*, 29(2), 151–175.

Rageh, O.S. and Koraim, A.S., 2010. Hydraulic performance of vertical walls with horizontal slots used as breakwater, *Coastal Engineering*, 57(8), 745–756.

Ramnarayan, S.K., Sannasiraj, S.A. and Sundar, V., 2020. Hydrodynamic characteristics of curved and vertical front face pile-supported breakwaters in regular waves, *Ocean Engineering*, 216, 108105.

Rodríguez, M. and Spinneken, J., 2016. A laboratory study on the loading and motion of a heaving box, *Journal of Fluids and Structures*, 64, 107–126.

Sharifahmadian, A. and Simons, R.R., 2014. A 3D numerical model of nearshore wave field behind submerged breakwaters, *Coastal Engineering*, 83, 190–204.

Shugan, I.V., Hwung, H.H., Yang, R.Y. and Hsu, W.Y., 2012. Elastic plate as floating wave breaker in a beach zone, *Physics of Wave Phenomena*, 20(3), 199–203.

Sundar, V. and Subba rao, B.V.V., 2002. Hydrodynamic pressures and forces on quadrant front face pile supported breakwater, *Ocean Engineering*, 29(2), 193−214.

Tuković, Ž., Karač, A., Cardiff, P., Jasak, H. and Ivanković, A., 2018. Openfoam finite volume solver for fluid-solid interaction, *Transactions of FAMENA*, 42(3), 1–31.

Vijay, K.G., Nishad, C.S., Neelamani, S. and Sahoo, T., 2020. Gravity wave interaction with a wave attenuating system, *Applied Ocean Research*, 101, 102206.

Wang, G.Y., Wang, Y.X. and Li, G.W., 2005. Experimental study on a new kind of open type breakwaters, *Journal of Hydrodynamics*, 17(2), 228–233.

Wu, W.D., Zhong, H.S. and Huang, J., 2002. Factors influencing wave attenuation effectivness of pipe-tyre floating breakwaters, *Journal of Hohai University* (*Natural Sciences*), 30(5), 79−82. (in Chinese)